

The Dependence of Galaxy Formation on Cosmological Parameters: Can we distinguish the WMAP1 and WMAP3 Parameter Sets?

Jie Wang^{*}, Gabriella De Lucia, Manfred G. Kitzbichler, Simon D. M. White

Max-Planck-Institut für Astrophysik, Karl-Schwarzschild-Str. 1, D-85748 Garching, Germany

Accepted 2007 ???? ?. Received 2007 ???? ?; in original form 2007 ???? ?

ABSTRACT

We combine N -body simulations of structure growth with physical modelling of galaxy evolution to investigate whether the shift in cosmological parameters between the 1-year and 3-year results from the Wilkinson Microwave Anisotropy Probe affects predictions for the galaxy population. Structure formation is significantly delayed in the WMAP3 cosmology, because the initial matter fluctuation amplitude is lower on the relevant scales. The decrease in dark matter clustering strength is, however, almost entirely offset by an increase in halo bias, so predictions for galaxy clustering are barely altered. In both cosmologies several combinations of physical parameters can reproduce observed, low-redshift galaxy properties; the star formation, supernova feedback and AGN feedback efficiencies can be played off against each other to give similar results. Models which fit observed luminosity functions predict projected 2-point correlation functions which scatter by about 10-20 per cent on large scale and by larger factors on small scale, depending both on cosmology and on details of galaxy formation. Measurements of the pairwise velocity distribution prefer the WMAP1 cosmology, but careful treatment of the systematics is needed. Given current modelling uncertainties, it is not easy to distinguish the WMAP1 and WMAP3 cosmologies on the basis of low-redshift galaxy properties. Model predictions diverge more dramatically at high redshift. Better observational data at $z > 2$ will better constrain galaxy formation and perhaps also cosmological parameters.

Key words: methods: N -body simulations – galaxies: formation – galaxies: evolution – cosmology: theory

1 INTRODUCTION

Our current understanding of the cosmic evolution is based heavily on measurements of the Cosmic Microwave Background (CMB). The discovery of the CMB (Penzias & Wilson 1965) led to general acceptance of the Hot Big Bang theory, and further support came from the subsequent demonstration of its near-perfect black-body spectrum (Mather et al. 1990). The detection and continuing refinement of measures of angular structure in the CMB confirmed theoretical predictions for the growth of structure in flat cosmologies dominated by non-baryonic Cold Dark Matter (CDM) (Smoot et al. 1990; de Bernardis et al. 2000, 2002). The power spectrum of this structure encodes information about the values of the cosmological parameters, although degeneracies prevent a precise determination of all parameters from CMB data alone. By including con-

straints from other kinds of data, it becomes possible to constrain many cosmological parameters quite tightly. During the last decade, a growing body of such measurements have ushered in a new era of ‘precision cosmology’.

The first-year data from the Wilkinson Microwave Anisotropy Probe (WMAP) (Spergel et al. 2003) did much to establish Λ CDM, a flat CDM model with a cosmological constant, as the standard model for structure formation. In addition, they provided apparently precise estimates for a number of cosmological parameters. Two further years of WMAP data have significantly refined these estimates, leading to noticeable shifts in some of the best values (Spergel et al. 2007). The most important differences are a reduction in optical depth to the last scattering surface (τ), a lower value for the amplitude of matter fluctuations on $8 h^{-1}$ Mpc scale (σ_8), a reduction of the scalar spectral index on primordial perturbations (n), and a lowering of the total matter density (Ω_m).

Several studies prior to the latest WMAP results

* Email: wangjie@mpa-garching.mpg.de

suggested a lower value for σ_8 . These looked at evolution in the abundance of galaxy clusters (Borgani et al. 2001; Schuecker et al. 2003), and at constraints from the abundance and clustering of low-redshift galaxies in combination with observed cluster mass-to-light ratios (van den Bosch et al. 2003; Tinker et al. 2005). Parameter estimates from these methods are partially degenerate in σ_8 and Ω_m and other studies, notably of cosmic shear, have tended to give conflicting indications (e.g. Massey et al. 2007; Benjamin et al. 2007; Hoekstra et al. 2006). Recent studies on giant arc statistics (Li et al. 2006) also suggest that low values of σ_8 may be difficult to reconcile with the observations. It is only the shrinking of the allowed parameter region forced by the new WMAP data that has persuaded much of the astronomical community to prefer a “standard” model with a lower value of σ_8 . It should be remembered, however, that including parameters beyond the usual minimal set significantly relaxes constraints, so that both first- and third-year WMAP parameter sets should probably be treated as plausible.

Modifications of the cosmological parameters of the kind discussed above can significantly affect the formation and evolution of structure. Recent studies have discussed the implications of WMAP third-year results for the formation of the first stars and black holes, and for the reionization of the intergalactic medium (Gao et al. 2006; Alvarez et al. 2006; Popa 2006; Lewis et al. 2006; Iliev et al. 2007), finding significantly later formation and reionization than previously thought.

The present paper investigates the impact of this delay on the observed properties of galaxies, both at low and at high redshift. We combine high-resolution N -body simulations with semi-analytic modelling techniques to simulate the evolution of the galaxy population (Springel et al. 2005; Croton et al. 2006; De Lucia & Blaizot 2007). Our paper is organised as follows: the N -body simulations and the semi-analytic modelling assumptions are described in sections 2 and 3. In section 4 we discuss the formation of dark matter structures in cosmologies with first-year and third-year WMAP parameters, while in section 5 we compare simulations of the evolution of the galaxy population in these two cosmologies. Finally, in section 6 we summarise and discuss our findings. For the convenience of the reader we also provide an appendix containing an analytic comparison of evolution in the abundance and clustering of dark halos in our two cosmologies, based on the formulae of Mo & White (2002)

2 THE SIMULATIONS

We have carried out two simulations of the growth of structure in a Λ CDM Universe using the cosmological parameter sets listed in Tab. 1. The cosmological parameters used for our WMAP1 simulation are derived from a combination of first-year WMAP results (Spergel et al. 2003) with the 2dFGRS galaxy power spectrum (Colless et al. 2001), and correspond to those used for the *Millennium Simulation* (MS; Springel et al. 2005). Our WMAP3 simulation adopts cosmological parameters derived from a combination of third-year WMAP data on large scale, and Cosmic Background Imager (CBI) and extended Very Small Array (VSA) data

Table 1. Cosmological parameters of the two simulations used in this study. Ω_m , Ω_Λ , Ω_b are the density of matter, dark energy and baryons respectively. σ_8 and n are the amplitude of the mass density fluctuations, and slope of initial power spectrum. The Hubble constant is parameterised as $H_0 = 100 h \text{ km s}^{-1} \text{ Mpc}^{-1}$.

	WMAP1	WMAP3
Ω_m	0.25	0.226
Ω_Λ	0.75	0.774
Ω_b	0.045	0.04
σ_8	0.9	0.722
h	0.73	0.743
n	1	0.947

on small scale (Spergel et al. 2007). We note that, among the different sets of cosmological parameters consistent with the third-year WMAP data and other observational data, we have chosen to look at the one which differs the most from the parameters of our WMAP1 simulation.

The most significant difference between the two sets of parameters listed in Table 1 is in the lower value of σ_8 adopted for the WMAP3 simulation. Our WMAP1 and WMAP3 cosmologies also differ in the scalar spectral index of primordial density perturbations ($n = 1 \rightarrow 0.947$), and in the matter density ($\Omega_m = 0.25 \rightarrow 0.226$). As noted above, a number of recent studies have shown that this change in cosmology results in a significant delay of structure formation in the WMAP3 case in comparison to WMAP1. We will discuss this in more detail in the following section.

The numerical parameters used for our simulations are listed in Table 2. The mass and force resolution are the same as used for the MS, while the volume is a factor 64 smaller. We have stored the data at the same 64 output times as in the MS. These are approximately logarithmically spaced between $z = 20$ and $z = 1$ and approximately linearly spaced in time thereafter. Friends-of-friends (FOF) group catalogues were computed on the fly for each snapshot, and the algorithm SUBFIND (Springel et al. 2001) was employed to decompose each FOF group into a set of disjoint substructures. As in Springel et al. (2005), only substructures which retain at least 20 bound particles after a gravitational unbinding procedure are considered to be genuine substructures. Substructure catalogues are then used to construct detailed merger history trees that provide the basic input needed for the semi-analytic model described in the next section. We refer to Springel et al. (2005) for more details of the merger-tree construction. Both our simulations were run using the tree-based parallel code GADGET2 (Springel 2005). The initial power spectra were generated using CMBFAST (Seljak & Zaldarriaga 1996) with the cosmological parameters listed in Tab. 1 as input. The Fourier modes of the initial density field in the two cases were identical except for the amplitude adjustment needed to reproduce the correct power spectrum. Thus structures correspond closely in the two cases.

Fig. 1 shows the power per decade in the linear initial conditions of our WMAP1 (blue) and WMAP3 (red) simulations. The significantly lower value of σ_8 in the WMAP3 case reduces the overall normalisation. In addition, the red tilt in the primordial power spectrum index makes the differ-

Table 2. Numerical parameters of our two simulations. L is the box size, n_p is the particle number, ϵ is the softening length, and m_p is the particle mass.

L	n_p	ϵ	$m_p(\text{WMAP1})$	$m_p(\text{WMAP3})$
125 Mpc h^{-1}	540 ³	5 kpc	8.61e8 $M_\odot h^{-1}$	7.78e8 $M_\odot h^{-1}$

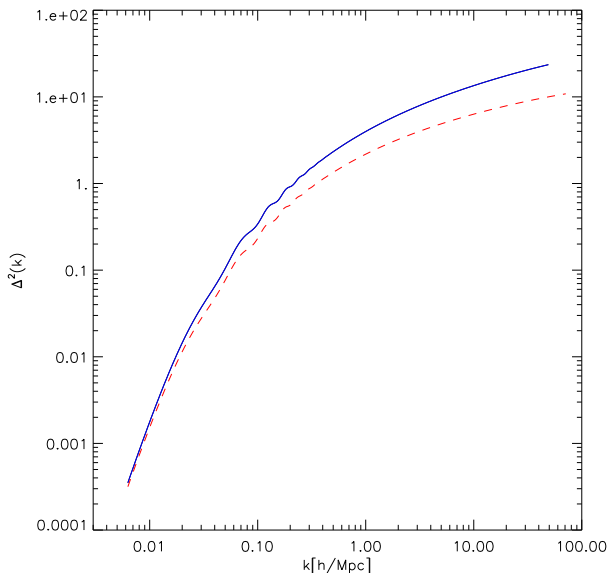


Figure 1. The power spectra of our two simulations: WMAP1 (blue solid) and WMAP3 (red dashed). These were generated using CMBFAST with the cosmological parameters listed in Tab. 1. The quantity plotted is $\Delta^2(k) \propto k^3 P(k)$.

ence greater on small scales than on large scales. Indeed, on the scales responsible for the low ℓ microwave background fluctuations the two power spectra are almost the same, reflecting the fact that they are both required to fit observed CMB fluctuations on these scales. Conversely, the suppression of power is particularly significant on the small scales responsible for the formation of the first nonlinear structures.

3 THE SEMI-ANALYTIC MODEL

In this paper we use the galaxy formation model described in De Lucia & Blaizot (2007) which is based on the WMAP1 cosmology and builds on previous work by the “Munich” galaxy formation group (Kauffmann et al. 1999a; Springel et al. 2001; De Lucia et al. 2004; Springel et al. 2005; Croton et al. 2006). Although not in perfect agreement with all aspects of the local galaxy population (see, for example, Weinmann et al. (2006)), this model does quite a good job of reproducing the observed relations between stellar mass, gas mass, and metallicity (De Lucia et al. 2004), the observed luminosity, colour, and morphology distributions (Croton et al. 2006; De Lucia et al. 2006) and the observed two-point correlation functions (Springel et al. 2005).

Kitzbichler & White (2007) have recently shown that it also agrees reasonably well with the observed galaxy luminosity and mass functions at high redshift. We refer the reader to the original papers for a full description of the numerical implementation, and of the physical processes modelled. In the following, we summarise briefly the treatment of those physical processes for which we needed to change the efficiency parameters in order to maintain agreement with observations of the local galaxy population when we switch from WMAP1 to WMAP3 (see Table 3 and Sec. 5).

In the semi-analytic model we use in this work, star formation is assumed to occur at a rate given by:

$$\dot{m}_* = \alpha_{\text{SF}}(m_{\text{cold}} - m_{\text{crit}})/t_{\text{dyn,disc}} \quad (1)$$

where m_{cold} and $t_{\text{dyn,disc}}$ are the cold gas mass and the dynamical time of the galaxy, defined as the ratio between the disk radius and the virial velocity, m_{crit} corresponds to a critical value for the gas surface density (Kennicutt 1998; Kauffmann 1996; Mo et al. 1998), and α_{SF} controls the efficiency of the transformation of cold gas into stars when the gas surface density is above the critical value. (See Croton et al. (2006) for more detailed descriptions of the implementation of this process and of the feedback processes described below.)

Massive stars explode as supernovae shortly after a star formation event and are assumed to reheat a gas mass that is proportional to the mass of stars formed (based on the observations of Martin 1999):

$$\Delta m_{\text{reheated}} = \epsilon_{\text{disk}} \Delta m_*, \quad (2)$$

Again following Croton et al. (2006), we write the energy released by an event which forms a mass Δm_* in stars as:

$$\Delta E_{\text{SN}} = 0.5 \epsilon_{\text{halo}} \Delta m_* V_{\text{SN}}^2, \quad (3)$$

where $0.5 V_{\text{SN}}^2$ is the mean supernova energy injected per unit mass of newly formed stars, and ϵ_{halo} represents the efficiency with which this energy is able to convert cold interstellar medium into hot, diffuse halo gas. The amount of gas that leaves the dark matter halo in a “super-wind” is determined by computing whether excess SN energy is available to drive the flow after reheating of material to the halo virial temperature.

As in Kauffmann & Haehnelt (2000), black holes are formed and fuelled during mergers:

$$\Delta m_{\text{BH}} = \frac{f'_{\text{BH}} m_{\text{cold}}}{1 + (280 \text{ km s}^{-1} / V_{\text{vir}})^2} \quad (4)$$

We assume here that black holes grow during both major and minor mergers, and that the efficiency of gas accretion onto the black hole scales with the baryonic mass ratio of the merging galaxies:

$$f'_{\text{BH}} = f_{\text{BH}} \times (m_{\text{sat}} / m_{\text{central}}) \quad (5)$$

This is the primary process driving the growth of the total mass in supermassive black holes. Individual black holes can also gain mass through merging when their host galaxies merge.

Finally, we use the model by Croton et al. (2006) to describe heating by centrally located AGN in massive groups and clusters. This process is assumed to be associated with “radio mode” outflows which suppress cooling flows and thus

the condensation of gas onto the central galaxies. The process is assumed to occur whenever a massive black hole finds itself at the centre of a static hot gas halo. During this phase, the accretion rate onto the central supermassive black hole is taken to be:

$$\dot{m}_{\text{BH,R}} = \kappa_{\text{AGN}} \left(\frac{m_{\text{BH}}}{10^8 M_{\odot}} \right) \left(\frac{f_{\text{hot}}}{0.1} \right) \left(\frac{V_{\text{vir}}}{200 \text{ km s}^{-1}} \right)^3, \quad (6)$$

where m_{BH} is the black hole mass, f_{hot} is the fraction of the total halo mass in the form of hot gas, V_{vir} is the virial velocity of the halo, and κ_{AGN} is efficiency parameter with units of $M_{\odot} \text{ yr}^{-1}$. The energy released during this accretion process is used to reduce the cooling flow. Croton et al. (2006) showed that this results in complete suppression of cooling in relatively massive haloes and groups. The process starts being effective at a mass scale that evolves as a function of redshift as shown in their Fig. 7.

In our simulation scheme, haloes (and the galaxies within them) are followed even after they are accreted onto larger systems. The dynamics of such a satellite subhalo is followed explicitly by the N-body simulation until tidal stripping causes its mass to fall below the resolution limit of the simulation (Ghigna et al. 2000; De Lucia et al. 2004; Gao et al. 2004). When this happens, we estimate a survival time (t_{merge}) for the associated galaxy using its current orbit and the classical dynamical friction formula of Binney & Tremaine (1987). Once this time has elapsed, the galaxy is assumed to merge onto the central galaxy of its current halo. While it still survives it is assumed to follow the particle which was the most bound particle of the subhalo at the last time it was identified. De Lucia & Blaizot (2007) found that increasing the merging time by a factor of 2 slightly improves the fit to observed luminosity function. Such an increase has other effects which De Lucia & Blaizot (2007) did not study, for example, it increases the amplitude of small-scale galaxy correlations by about a factor of 2 at $r < 100$ kpc. Others authors have claimed that this merging time should be effectively set to zero, so that such ‘‘orphan’’ galaxies lose their identity at the same time as their subhaloes (Conroy et al. 2007). Here we leave this issue for detailed study in future work and simply consider the pre-factor to be used for t_{merge} as a free parameter.

4 FORMATION OF DARK MATTER STRUCTURES

Figure 2 shows the dark matter distribution at $z = 0$ within a slice $20 \text{ Mpc } h^{-1}$ thick cut from the full volume of our simulations. The WMAP1 model is on the left and the WMAP3 model on the right. The projection is colour-coded by density and provides a visual illustration of the delay of structure formation in the lower σ_8 model. Although the overall structure is very similar, it is clear that massive haloes lying at the nodes of the cosmic web are in a more advanced stage of merging in the WMAP1 case than in the WMAP3 case.

The differing fluctuation amplitudes of the two simulations translate into a systematic difference between their halo mass functions. This is illustrated in Fig. 3 where we compare the cumulative number density of haloes for the two cases (blue for WMAP1, red for WMAP3). In addition, we show the corresponding function for the much larger Mil-

lennium Simulation (green) which used our WMAP1 cosmological parameters. It agrees very well with the smaller WMAP1 simulation of this paper. At $z = 0$, the most massive haloes in our WMAP3 simulation are about 1.5 times less massive than their counterparts in the WMAP1 simulation. The number of haloes more massive than $10^{13} M_{\odot} h^{-1}$ is ~ 25 per cent smaller in the WMAP3 case than in the WMAP1 case. These differences increase at higher redshift. At $z \sim 6$ (i.e. at the end of the reionization epoch) the most massive haloes in the two simulations differ by about a factor of 5 in mass.

We recall that the main differences between the cosmological parameters used in the two simulations are the lower value of σ_8 and the redder primordial power spectrum index n in the WMAP3 case. As shown in Fig. 1, these combine to produce a substantial suppression of small-scale power. This has important implications for the formation of the first objects and for the star formation history at early times. Gao et al. (2006) studied this problem using high-resolution cosmological simulations with a smoothed particle hydrodynamics treatment of baryonic processes. They found a much lower abundance of potentially star-forming haloes at high redshift for WMAP3 than for WMAP1. This reduction in the number of ‘mini-haloes’ at $z \sim 10$ was also discussed by Reed et al. (2007) using analytic models to explore the dependence on cosmological parameters. For fluctuation amplitudes at the WMAP1 level, very efficient production of UV radiation is needed to reionize the intergalactic medium by $z \sim 15$, as required by the WMAP1 value for the electron scattering optical depth τ (e.g. Ciardi et al. 2003). Interestingly, the delay in structure formation in a WMAP3 Universe is such that *equally* efficient UV production is needed to reionize by $z \sim 10$, as inferred from the WMAP3 value of τ (Alvarez et al. 2006).

Fig. 4 shows $z = 0$ autocorrelation functions in our WMAP1 and WMAP3 simulations for the dark matter (in the top panel) and for all dark matter substructures identified by SUBFIND (in the bottom panel; this corresponds to all self-bound (sub)haloes with more than 20 simulation particles). The difference in fluctuation amplitude causes the correlation strength to be almost a factor of two smaller in the WMAP3 case than in the WMAP1 case on scales below a few Mpc. Curiously, however, this decrease is almost completely compensated by an increase in the (sub)halo bias, so that the 2-point correlation functions for subhaloes are almost identical in the two cases. There is a slight residual offset on scales $0.5 \text{ Mpc } h^{-1} \lesssim r \lesssim 5 \text{ Mpc } h^{-1}$. As we will see below, this results in very similar galaxy correlation functions being predicted in the two cases.

5 GALAXY FORMATION

In this section we analyse galaxy populations simulated using the semi-analytic framework presented in Sec. 3. Table 3 lists the combinations of semi-analytic parameters for which we will show detailed results. Model A is the parameter set used by De Lucia & Blaizot (2007) for the Millennium Simulation. As expected, this also gives good agreement with observation for our WMAP1 simulation. Models B and C are parameter combinations that, as we show below, pro-

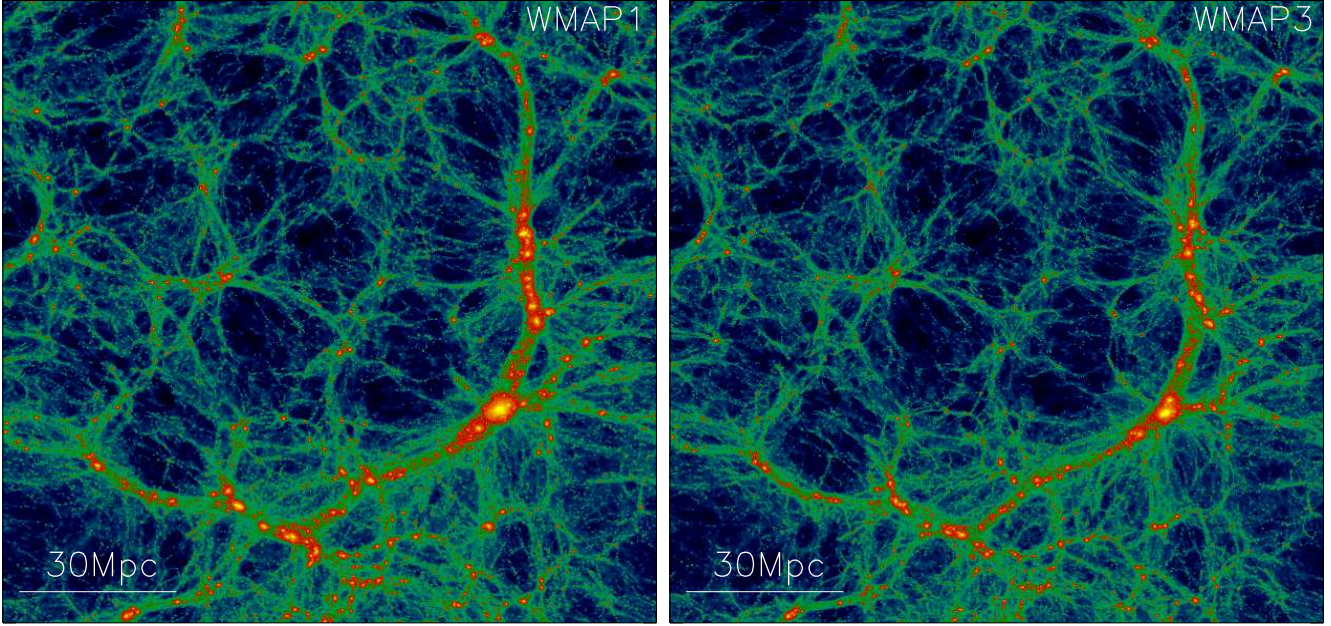


Figure 2. Redshift zero distribution of dark matter within a slice of thickness $20 \text{ Mpc } h^{-1}$ through our two simulations, WMAP1 (left) and WMAP3 (right).

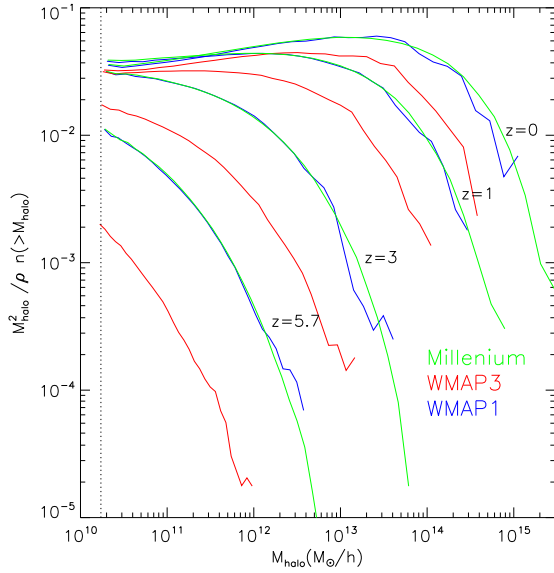


Figure 3. Cumulative halo number density as a function of halo mass and redshift. Results for the WMAP3 and WMAP1 simulations are represented by red and blue curves respectively. Results for the Millennium Simulation are shown in green. The halo abundance is multiplied by M^2 in order to reduce the dynamic range of the ordinate.

duce a similar agreement with local data for the WMAP3 cosmology.

Model B has the same star formation efficiency as model A (α_{SF}), but lower supernova feedback efficiency (ϵ_{halo} and ϵ_{disk}), and lower AGN feedback efficiency (κ_{AGN}). For this model, we have also eliminated the pre-factor of 2 which

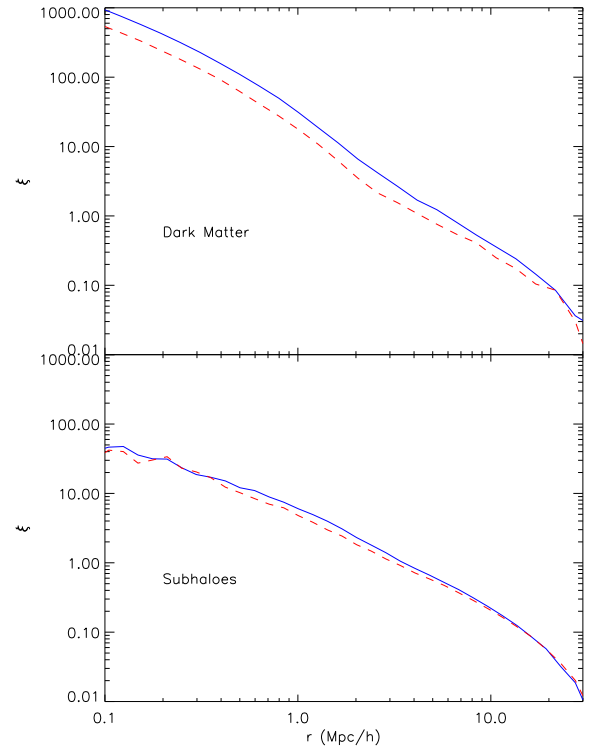


Figure 4. Autocorrelation functions at $z = 0$ for dark matter (top panel) and for all subhaloes with at least 20 particles (bottom panel). Blue solid and red dashed curves show results for our WMAP1 and WMAP3 simulations respectively.

Table 3. Principal parameters of our galaxy formation models (see text for details).

	A	B	C
α_{SF}	0.03	0.03	0.07
ϵ_{halo}	0.35	0.2	0.28
ϵ_{disk}	3.5	3	4.5
κ_{AGN}	7.5e-6	6.5e-6	1.2e-5
f_{BH}	0.03	0.03	0.05
t_{merge}	$2 \times t_{\text{friction}}$	t_{friction}	$2 \times t_{\text{friction}}$
Best for	WMAP1	WMAP3	WMAP3

De Lucia & Blaizot (2007) introduced in the definition of the merging time. In contrast, in model C, we double the star formation efficiency (relative to model A) in order to compensate for the delay in structure formation, but this must be compensated by much higher feedback efficiencies (both from supernovae and from AGN) to prevent the overproduction of stars at late times. For this model we keep the pre-factor of 2 in the definition of the merging times of satellite galaxies. We also increase the efficiency of accretion onto black holes during mergers (which increases the effectiveness of the ‘radio’ mode - see Eq. 6). In the following, we will show that models B and C give similar $z = 0$ results for the WMAP3 cosmology, and that these resemble the results of model A for the WMAP1 simulation. This shows that there are at least two independent way to ‘compensate’ for the delay in the structure formation within this physical framework: we can decrease feedback on all scales while keeping the same star formation efficiency (model B), or we can increase both the star formation efficiency and the feedback efficiency on all scales (model C).

In the following sections we discuss how the predictions of our three models compare to observational data both in the local Universe and at high redshift.

5.1 Low-redshift Luminosity Functions

Figure 5 compares observational estimates of the K-band luminosity function of nearby galaxies to predictions from our three galaxy formation models (differentiated by colour) applied to each of our two simulations (differentiated by line type). In both cosmologies models B and C give almost identical results, while model A predicts fewer galaxies at bright luminosities ($M_K < -22$) by a factor that varies from 1.3 to 3. The inset in Fig. 5 repeats the figure showing only results from model A applied to our WMAP1 simulation and from models B and C applied to our WMAP3 simulation. This shows all three models to produce similarly good fits to the observations around and above the ‘knee’. All three models show an excess of galaxies fainter than $M_K - 5 \log h \sim -22$ with respect to the Cole et al. (2001) data, although they lie below the luminosity function given by Huang et al. (2003). This possible excess is more pronounced in model A. In the following we will only discuss results from our ‘best’ models (i.e. model A for our WMAP1 simulation and for the Millennium Simulation, models B and C for our WMAP3 simulation; in the following we denote these as A1, MSA, B3 and C3).

Figure 6 compares model galaxy luminosity functions in

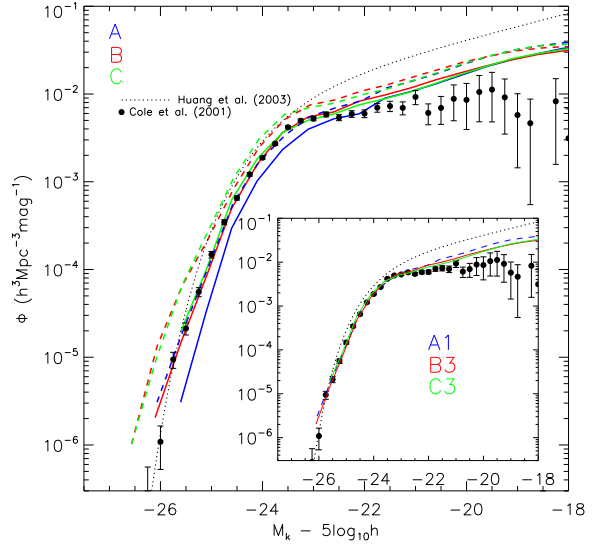


Figure 5. K-band luminosity function for the three galaxy formation models and the two cosmologies simulated in this study. Results from models A, B, and C are shown in blue, red and green respectively. Solid and dashed lines correspond to our WMAP3 and WMAP1 simulations respectively. The black symbols with error bars show the observational determination by Cole et al. (2001), while the black dotted curve shows the measurements of Huang et al. (2003). The inset repeats the figure but shows results only from model A applied to WMAP1 and from models B and C applied to WMAP3.

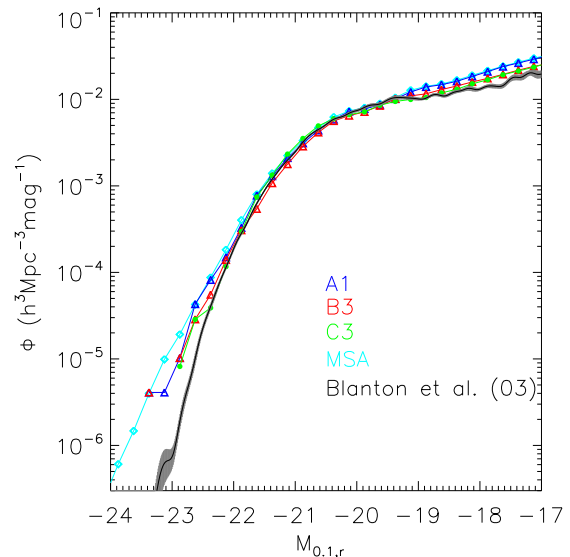


Figure 6. Galaxy luminosity function at SDSS $r_{0.1}$ band. Coloured lines show predictions from the three ‘good’ models of this paper. We also plot results from model A applied to the Millennium Simulation. The black curve with an error band corresponds to the observational measurement from Blanton et al. (2003).

the Sloan Digital Sky Survey (SDSS) r-band to observational measurements from the SDSS itself. Here the observational uncertainties are much smaller than for the K-band luminosity function of Fig. 5. Since the observed absolute magnitudes quoted by Blanton et al. (2003) are band-shifted to $z = 0.1$, we also correct our simulated r-band absolute magnitude to this redshift using their K-correction code. Fig. 6 shows all our “good” models to agree very well with the observational data, particularly around the knee of the luminosity function ($-22 < M_r < -19$). All models overpredict the abundance of faint galaxies, although the problem appears significantly less dramatic here than in Fig. 5. In all models the rarest and most luminous galaxies are also too bright by 0.2 to 0.6 magnitudes. This problem may be, at least partially, due to our assigning light to these objects which should be part of the intracluster light of the groups or clusters of which they are the central galaxies (see also Conroy et al. (2007)).

5.2 The Tully-Fisher Relation

In Fig. 7, we compare the Tully-Fisher relation for our model galaxies to the observational determination by Giovanelli et al. (1997). Green symbols show all model central galaxies with $1.5 < M_{B,\text{bulge}} - M_{B,\text{total}} < 2.6$ where $M_{B,\text{bulge}}$ and $M_{B,\text{total}}$ are the absolute magnitude of the bulge and the total B-band magnitude, respectively. This selection is made in order to isolate Sb/c spirals as in the observed sample of Giovanelli et al. (1997). The mean observational relation is shown by a solid blue line in the figure, with the corresponding 1σ scatter indicated by the dashed lines. The relation of Giovanelli et al. is already corrected for internal extinction. We therefore do not include dust effects when predicting I-band magnitudes for this plot. Red lines in each panel show a linear fit to the model results. The top panel of Fig. 7 demonstrates that model A1 reproduces both the slope and the zero-point of the observed relation (as also shown in Croton et al. 2006). Models B3 and C3 exhibit a substantially brighter zero-point than observed. This occurs because fitting the observed luminosity function within the less evolved halo mass function of the WMAP3 cosmology (see Fig. 2) requires us to put galaxies of given luminosity at the centre of lower mass halos than in the WMAP1 case.

Finding theoretical models which simultaneously fit both the observed luminosity functions and the observed Tully-Fisher relation has always been difficult (e.g. Cole et al. 2000). The results in Fig. 7 show that this remains true. Note, however, that it is uncertain how best to extract quantities from our models for comparison with the observational data. For example, we assume here that W (the measured HI linewidth) is twice the maximum circular velocity of the galaxy’s dark halo, as measured directly from the simulation and without any correction for the effects of the baryonic mass of the galaxy. This is a rough assumption which may be systematically in error. In particular, if galaxy formation results in a maximum disk rotation velocity which is significantly and systematically above this value, the population of galaxies in our WMAP3 model could be reconciled with the observations. Changing the transformation between these two velocities can change the slope and zero-point, or introduce curvature into the model Tully-Fisher relation. Semi-analytic models provide robust estimates for

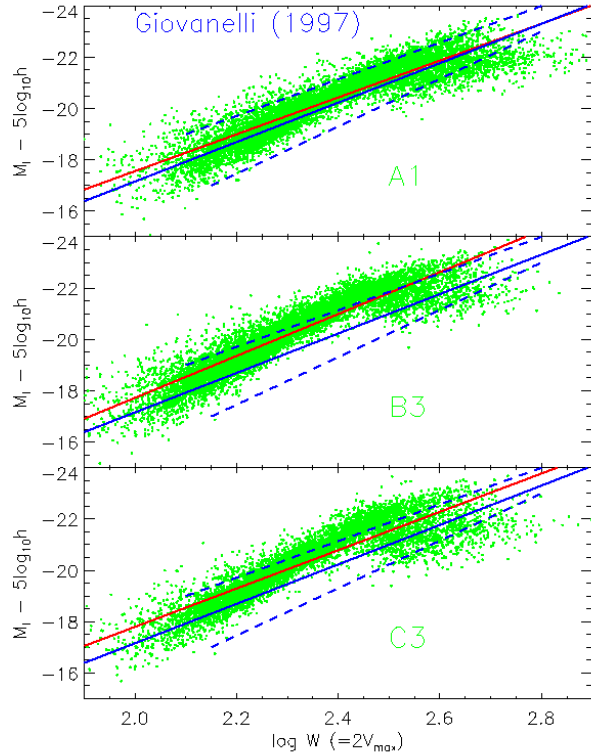


Figure 7. Tully-Fisher relation for spiral galaxies in our three models. We show only central galaxies with $1.5 < M_{B,\text{bulge}} - M_{B,\text{total}} < 2.6$, and we approximate the observed HI linewidth by twice V_{max} for the dark halo, as measured directly in our simulations. Red lines are linear fits to the model results. The blue solid line shows the mean observational relation by Giovanelli et al. (1997), with blue dashed lines indicating the scatter in this relation.

the locations, velocities and global properties (luminosity, colour, stellar mass, etc.) of galaxies, but become less reliable when quantities (such as W) which depend sensitively on the internal structure of the galaxies must be predicted (see also the discussion in Somerville & Primack 1999).

5.3 Mass-to-Light Ratios of Clusters

In Fig. 8, we plot SDSS $r_{0.1}$ band mass-to-light ratios ($M/L_{r,0.1}$) for individual clusters with $M \geq 10^{14} M_{\odot}$ (symbols) and the running median value over the full resolved mass range (solid lines). Both M and $L_{r,0.1}$ are computed within R_{200} , defined as the radius within which the mean mass overdensity is 200 times the critical value. Blue, red and green are used for models A1, B3, and C3 respectively. Cyan is used for the model MSA which provides a larger number of clusters than the smaller simulations used in our study. The black horizontal line and hatched area show the region occupied by the observational data in Carlberg et al. (1996, see Tinker et al. 2005 for details on the conversion to the SDSS $r_{0.1}$ band). Our models exhibit a very weak mass dependence over the observed mass range and agree reasonably well with the observational measurements. The differences between the two cosmological models, and between the

two galaxy formation models for same WMAP3 cosmology are small, even at small masses where van den Bosch et al. (2007) found a more pronounced decrease in the mass-to-light ratio for WMAP3 cosmology with respect to WMAP1.

It is interesting to compare our results with those based on halo occupation distribution (HOD) models. van den Bosch et al. (2003) found that their conditional luminosity function (CLF) model was unable to fit the observed mass-to-light ratios of clusters in a cosmology with WMAP1 parameters, and they argued strongly in favour of a cosmology with a lower value of σ_8 , similar to that subsequently preferred by WMAP3. Once their models are constrained to fit the observed luminosity and correlation functions of galaxies, they find $\langle M/L \rangle$ to vary roughly as σ_8^2 on cluster scales. Tinker et al. (2005) found a similarly strong dependence of the mass-to-light ratio on σ_8 using an HOD model which differed in detail and which they constrained with different observational data. M/L predictions from these models are shown in Fig. 8 by the horizontal dashed and dotted lines (blue and red are used for WMAP1 and WMAP3 respectively). Predictions from van den Bosch et al. (2003) were obtained by converting their B-band estimates to the SDSS $r_{0.1}$ band using the conversion factor adopted in Tinker et al. (2005). These authors convert the mean B-band mass-to-light ratio $\langle M/L_B \rangle = 363h(M/L)_\odot$ of Carlberg et al. (1996) to $\langle M/L_{r,0.1} \rangle = 359h(M/L)_\odot$ in the SDSS $r_{0.1}$ band. Thus we multiply the results of van den Bosch et al. (2003) by a factor of $359/363 = 0.988$. Fig. 8 shows that the mass-to-light ratio dependence on σ_8 in our models is much weaker than in the two HOD models mentioned above. This is surprising since our models are also a good fit to the observed galaxy luminosity functions, and fit observed correlation functions moderately well, at least on large scale (see below).

In Fig. 8, we also show as a black solid line the average mass-to-light ratio predicted by the physically based HOD model presented in Wang et al. (2006). These authors use the same positions and velocities for galaxies as our semi-analytic model (taken directly from the Millennium Simulation) but adopt simple parametrized functions to relate the star formation rates of galaxies to the mass and location (satellite or central) of their parent subhalo. The parameters of these functions are then minimized in order to optimize the fit to the observed luminosity function and luminosity-dependent correlation functions. The cluster mass-to-light ratios predicted by this model are higher than those in any of the semi-analytic models in our study, and are reasonably close to the predictions of van den Bosch et al. (2003) and Tinker et al. (2005) for a WMAP1 cosmology (the cosmology adopted in the Millennium Simulation). Comparing the model of Wang et al. (2006) in detail to the MSA model, we find that the larger mass-to-light ratio on cluster scales is due to systematic lower central galaxy luminosities (by a factor ~ 2) in the HOD model. We note that De Lucia & Blaizot (2007) found reasonable agreement when comparing this same MSA model to the observed K-band magnitudes of brightest cluster galaxies (BCGs). We note also that precise measurements of BCGs luminosities are complicated by the intrinsic difficulty in separating the contribution of the cD envelope (Schombert 1988; Gonzalez et al. 2005; Zibetti et al. 2005). The three HOD

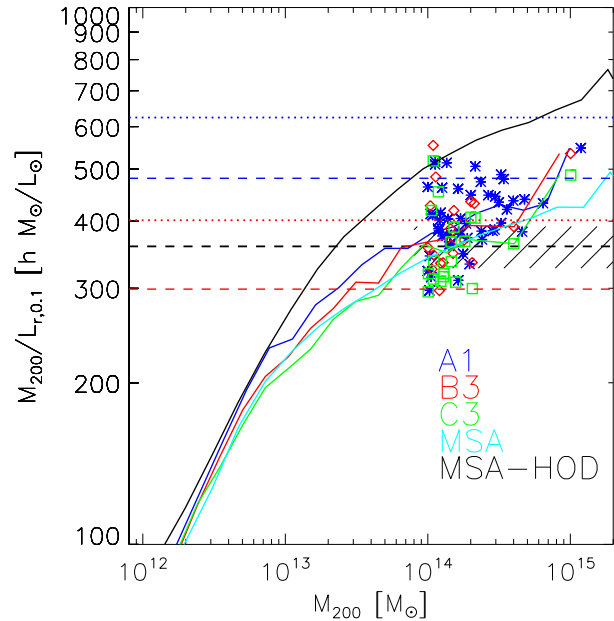


Figure 8. Mass-to-light ratios in the SDSS $r_{0.1}$ band as a function of halo mass. Symbols show results for the 48 (20) clusters with mass $M > 10^{14} M_\odot$ in our WMAP1 (WMAP3) simulation. Solid lines show a running median over a wider range of halo masses. Blue, red, green and cyan are used for models A1, B3, C3 and MSA respectively. The black solid curve refers to the HOD model of Wang et al. (2006) applied to the Millennium Simulation (MSA-HOD). The black dashed line and the hatched area show the region occupied by the observational data of Carlberg et al. (1996). The horizontal dotted and dashed lines show predictions for M/L of clusters $M > 10^{14} M_\odot$ from van den Bosch et al. (2003) and Tinker et al. (2005) respectively. In each case blue refers to the WMAP1 and red to the WMAP3 prediction.

models shown in Fig. 8 exhibit a stronger dependence on cosmology (in particular σ_8), but also a larger dependence on modelling details than do our semi-analytic models. It seems, therefore, that a good understanding of the consequences of modelling assumptions is needed before firm conclusions can be drawn about σ_8 or other cosmological parameters.

5.4 Pairwise Velocity Dispersion

Pairwise velocity dispersions (PVD) are a useful tool because of their strong sensitivity to the abundance of massive haloes (Mo et al. 1993; Jing & Börner 2004; Yang et al. 2004; Tinker et al. 2006). Fig. 3 shows that the present-day abundance of massive haloes with mass $\geq 10^{14} M_\odot/h$ in WMAP3 is almost 2.5 times lower than the corresponding abundance in WMAP1. This should be reflected in differences in the predicted PVD.

In Fig. 9, we present the dependence of PVD on SDSS $r_{0.1}$ luminosity for the three SA models used in this work. The black points with error bars show observational estimates from Li et al. (2007) obtained by modelling the full two-dimensional redshift-space correlations. In order to compare our model prediction with these data, we

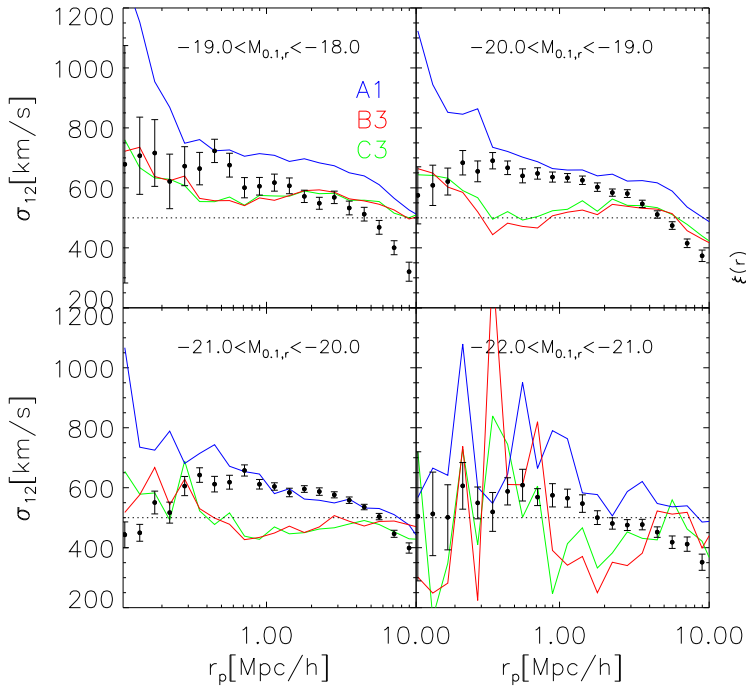


Figure 9. Pairwise velocity dispersions for our three SA models and for four luminosity bins in the SDSS $r_{0.1}$ band. Results from our three models are presented in blue (A1), red (B3) and green (C3). The black symbols with error bars are observational data from (Li et al. 2007). The horizontal dotted line corresponds to the $\sigma_{12} = 500\text{km/s}$

adopt the assumptions and modelling methods of Jing et al. (1998); Li et al. (2007) except that rather than constructing large mock catalogues, we measure directly both the 2-dimensional correlation function in redshift space ($\xi(r_p, \pi)$) and the real space correlation ($\xi(r)$) using the distant observer approximation for the former. Fig. 9 shows that model A1 produces higher dispersions (by $\sim 50 - 150\text{km/s}$) on all scales and for all luminosity subsamples than do the two WMAP3 models. Except for the faintest galaxies, model A1 also gives a better fit to the observational data. This agrees with Li et al. (2007) who compared their measurements to the model of Croton et al. (2006) which is very similar to our A1. Both WMAP3 models predict lower PVD than are observed, and they also seem to show a different slope. Thus, PVD observations seem to prefer a WMAP1 cosmology, as can be inferred from Jing & Börner (2004).

5.5 Galaxy Clustering

Figure 10 compares the 2-point correlation function of our model galaxies at redshift $z = 0$ to a recent measurement from the 2dFGRS (Hawkins et al. 2003). Solid colored lines show predictions from our three “good” models (blue for model A1, red and green for models B3 and C3 respectively). For each model there are about 17000 galaxies with $M_k < -23$. This magnitude limit is just fainter than the knee in Fig. 5 so that most luminous galaxies are included. In order to estimate the cosmic variance in these estimates, we divide the *Millennium Simulation* galaxy catalogue of

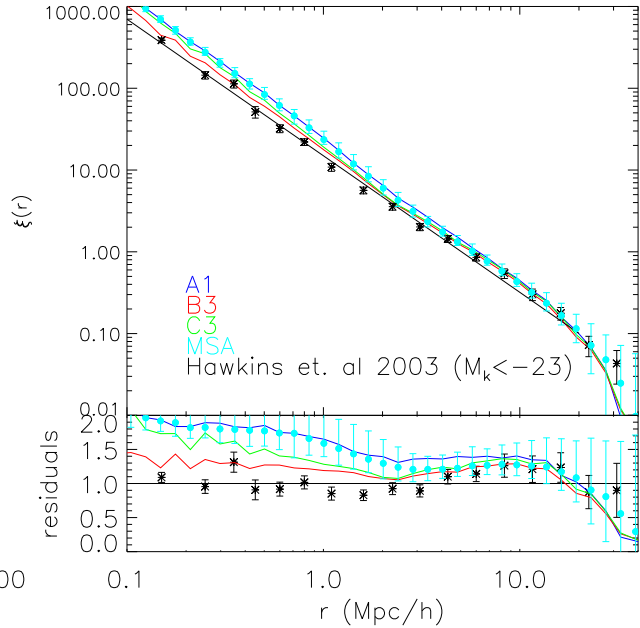


Figure 10. 2-point autocorrelation functions for luminous galaxies in K-band at $z = 0$. Solid colored curves show results for the three “good” models of this paper. The cyan symbols with error bars are predictions based on 64 small boxes (each with the volume of the simulations of this paper) cut from the Millennium Simulation catalogue of De Lucia & Blaizot (2007). Black symbols with error bars and the black solid line show observational estimates and a power law fit from the 2DFGRS (Hawkins et al. 2003). The residuals shown in the lower panel are calculated with respect to this power law fit.

De Lucia & Blaizot (2007) into 64 small boxes, each with the same volume as our new simulations, and then calculate the mean and scatter of the resulting 64 autocorrelation estimates. (We have taken care to eliminate edge effects when calculating correlations for galaxies within these sub-volumes.) Cyan symbols show the mean calculated in this way, while the error bars give the 10% to 90% range. Our models were not tuned to match observational measures of galaxy clustering, so the overall agreement with observations demonstrated by Fig.10 is encouraging.

We can also see that results from the three models converge on large scales ($\gtrsim 6h^{-1}\text{Mpc}$). On intermediate scales ($6h^{-1}\text{Mpc} \gtrsim r \gtrsim 1h^{-1}\text{Mpc}$), models B3 and C3 exhibit weaker clustering than model A1, agreeing better with the observational estimates. Interestingly, the 2-point correlation function of subhaloes (see Fig. 4) shows a similar offset between the models on these scales. On smaller scales ($r < 1h^{-1}\text{Mpc}$) the three models give different results – B3 agrees with the observational data to within the scatter found among the 64 Millennium data to samples, while C3 is marginally high and A1 is significantly high. Clearly clustering on these scales is quite sensitive to details of the galaxy formation physics.

It is also interesting that model A1 is significantly high compared to the mean of the Millennium results on scales between 2 and $8h^{-1}\text{Mpc}$, even though the two simulations

adopt the same galaxy formation physics within the same cosmology. This suggests that the particular realisation of a $L = 125h^{-1}\text{Mpc}$ box used in this paper overestimates clustering on these scales. Correcting for this would bring models B3 and C3 into excellent agreement with the observations for $r > 2h^{-1}\text{Mpc}$. In summary, all three models agree well with the data on the large scales that are sensitive to 2-halo correlations. Model B3 also agrees well with observation on smaller scales which are dominated by galaxy pairs within a common halo. C3 is slightly high on these scales and A1 is too high to be compatible with the observational data. We note, however, that there is a significant difference between B3 and C3 which are implemented on the same WMAP3 simulation. This emphasizes that small-scale galaxy correlations are very sensitive to details of the adopted galaxy formation physics and are unlikely to be useful for constraining cosmological parameters.

In Fig. 11 we study how galaxy correlations vary with luminosity, comparing the projected autocorrelations $w(r_p)$ from our models (solid coloured lines) with observational data from the SDSS (Li et al. 2006) (symbols with error bars). Results are shown for six magnitude bins from faint (top left) to bright (bottom right). Below each panel, we also show the ratio between the model and the observed estimates. The model projected correlation function has been determined by integrating the real space correlation function ($\xi(r)$) along the line-of-sight:

$$w(r_p) = 2 \int_0^\infty \xi(\sqrt{r_p^2 + r_{\parallel}^2}) dr_{\parallel} = 2 \int_{r_p}^\infty \xi(r) \frac{r dr}{\sqrt{r^2 - r_p^2}} \quad (7)$$

We note that if the integration is truncated at $r = 60\text{Mpc}/h$ (half the box size of our simulations) the resulting projected correlation function is reliable up to $\sim 10\text{Mpc}/h$. Because of the limited volume of our simulations, the two brightest magnitude bins contain only a few thousand and a few hundred galaxies respectively. Results for the fainter bins are based on much larger numbers of galaxies. The straight black line reproduced in each panel to facilitate comparison corresponds to the power-law:

$$\xi = (r/5 \text{Mpc } h^{-1})^{-1.8}$$

The results in this figure show reasonably good agreement between the models and the observations for $M_r < -20$, but significant overpredictions, particularly for model A1, at fainter absolute magnitudes and at large scales. The differences between model and observation show similar trends with pair separation for all the models, and are as large as the differences between the models themselves. On the basis of this comparison none of the models is obviously better or worse than the others. In particular, at bright magnitudes ($M_r < -20$) model A1 is a significantly better fit to the observations than either B3 or C3. This reproduces the trends which Li et al. (2007) found in their own comparison of SDSS correlation to the Millennium Simulation catalogue of Croton et al. (2006). This is the exact opposite of the conclusion drawn above from Fig. 10, suggesting that the level of agreement between different observational estimates of galaxy correlations is not yet good enough to distinguish between the various models we are discussing.

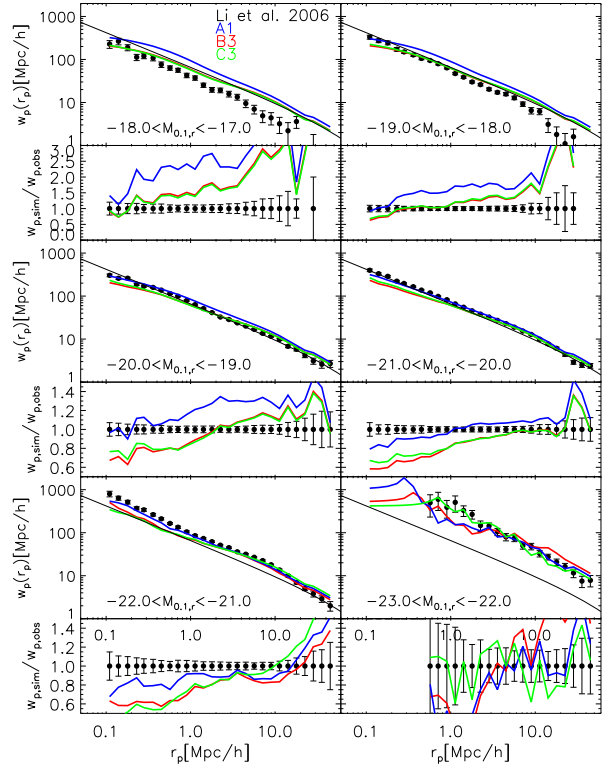


Figure 11. Projected correlation function w_p in the SDSS $r_{0.1}$ band. Coloured lines show results for our simulated galaxy catalogues. Black points are for the SDSS data (Li et al. 2006). Each pair of panels corresponds to a different absolute magnitude bin. The solid black line in the upper panel of each pair corresponds to the power-law: $\xi = (r/5 \text{Mpc } h^{-1})^{-1.8}$. The lower panel of each pair plots the ratio of model to observation, with error bars to indicate the uncertainty in the observational estimate.

5.6 Evolution to high redshift

Figure 12 shows how results from our models compare to the observed cosmic star formation rate density as a function of redshift. Symbols with error bars are a compilation of observational data taken from Fig. 12 of Springel & Hernquist (2003). Models B3 and C3 have quite similar star formation histories, although C3 lies above B3 by about 15 per cent at $z > 2$. This is due to the higher star formation efficiency used in model C. Model A1 provides much larger star formation rates than either B3 or C3 for $z > 1$ and lower star formation rates in the local Universe. The high redshift difference reflects the earlier formation of structure in the WMAP1 cosmology, while the difference at late times is a consequence of the requirement that all models produce the same total number of stars (as measured by the K-band luminosity function) in the present universe.

The most dramatic difference in Fig. 12 is that between the two cosmologies at the highest redshifts. For $z \sim 6$, the star formation rates are almost an order of magnitude lower in models B3 and C3 than in model A1. A related result, also visible in Fig. 12, is that the peak of the cosmic star formation history is shifted to lower redshift in the new cosmology: from $z \sim 3$ in model A1 to $z \sim 2$ in model

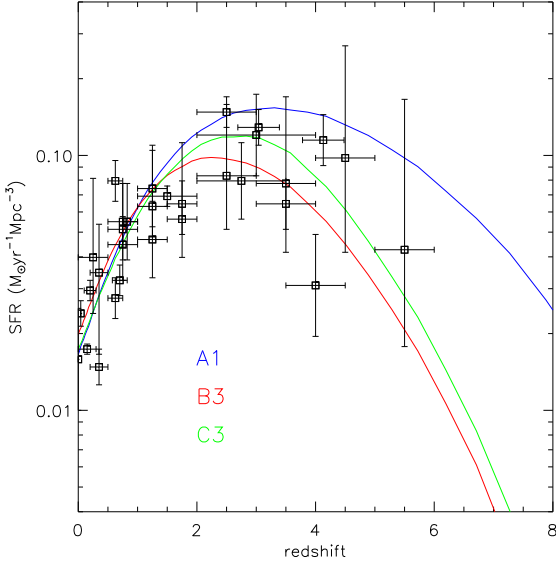


Figure 12. Cosmic star formation rate density as a function of redshift. Symbols with error bars are a compilation of observational data (taken from Fig. 12 of Springel & Hernquist 2003). The solid coloured curves show results from our ‘best’ models (see text for details).

B3 or to $z \sim 2.5$ in model C3. Fig. 12 suggests that measurements of the cosmic star formation rate at high redshift can potentially constrain models like those discussed here. Unfortunately, observational uncertainties (e.g. due to the use of different star formation estimators at different redshifts, and to the need for substantial dust corrections) are too large to discriminate reliably between our three models. In addition, these models are far from exhausting all physically plausible possibilities for the phenomenology of star formation and feedback, so the true theoretical uncertainty is undoubtedly larger than suggested by Fig. 12.

In a recent paper Kitzbichler & White (2007) compared results from the model discussed in De Lucia & Blaizot (2007) to a variety of observational data at high redshift. They found this model (which is identical to our model A) to give moderately good agreement with the observed luminosity and stellar mass functions of galaxies over a large redshift range. As shown in Fig. 12, the three models used in the present study have a significantly different behaviour at high redshift, so it is interesting to see if the observations can discriminate between them.

Our figures 13 and 14 correspond to figures 5 and 7 of Kitzbichler & White (2007) and show evolution with redshift of the rest-frame K-band luminosity function, and of the stellar mass function respectively. In Fig. 13, symbols with error bars show observational determinations from Cole et al. (2001); Pozzetti et al. (2003); Feulner et al. (2003); Saracco et al. (2006). The observational estimate in the local Universe from Cole et al. (2001) is repeated in the other panels as a black dashed line. Model results are shown as solid coloured lines (blue for A1, red for B3 and green for C3). Fig. 13 already showed all three models to agree nicely with local observations. At higher redshifts, the agreement is also reasonably good. All three seem to underpredict the

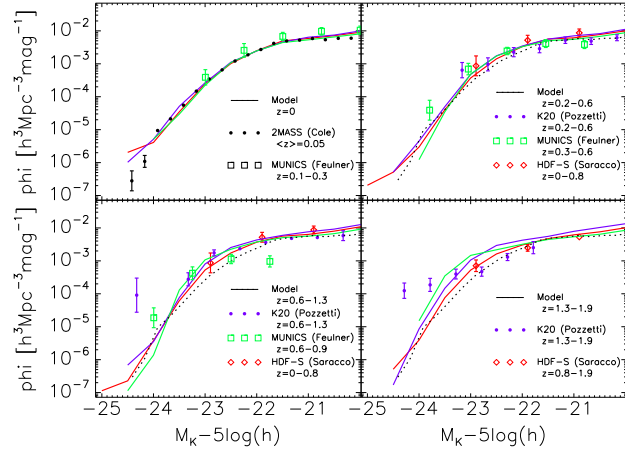


Figure 13. Rest-frame K-band luminosity functions for different redshift intervals. Model results are shown as solid lines (blue for A1, red for B3, and green for C3). Symbols with error bars show observational estimates from several surveys, as labelled in each panel. The low-redshift observational determinations of Cole et al. (2001) is repeated as a dotted black line in the other panels.

number of luminous galaxies in the highest redshift bin, but it should be kept in mind that the rest-frame K-band luminosities here have been extrapolated beyond the directly observed region, and so are quite uncertain (see the discussion in Kitzbichler & White 2007). Our three models start to show significant differences for $z > 1$. Note that model A1 lies between models B3 and C3 in this plot so that the differences are due mainly to galaxy formation physics rather than to cosmological parameters. They are, in any case, comparable to the uncertainties in the observations, so that significantly better data are required at these redshifts to put strong constraints on our models. Finally, we note that the error bars of Fig. 13 underestimate the true uncertainties as they do not include the effects of cosmic variance. These are particularly important when small regions of the sky are sampled - as is the case for the data in the highest redshift bin.

Fig. 14 shows the evolution of the galaxy stellar mass function for our three ‘‘good’’ models (coloured solid and dashed lines) and compares them with observational determinations from Cole et al. (2001); Drory et al. (2005); Fontana et al. (2006). As in Kitzbichler & White (2007), model results are shown both with (solid) and without (dashed) convolution with a normal distribution of standard deviation 0.25 dex, intended to represent measurement errors in $\log M_*$. The dashed black line in each panel repeats the local observational estimate by Cole et al. (2001). At redshifts beyond 1, model A1 predicts substantially more galaxies in the mass range $9 < \log(M_*/M_\odot) < 10.6$ than either of the models in the WMAP3 cosmology. This remains true at higher redshift for model B3, but not for model C3. For $\log(M_*/M_\odot) > 10.8$ models A1 and C1 predict similar numbers of massive galaxies at all redshifts. The increased star formation efficiency in model C as compared to model A clearly compensates for the lower σ_8 in the WMAP3 cosmology. This demonstrates that even at high redshift it may

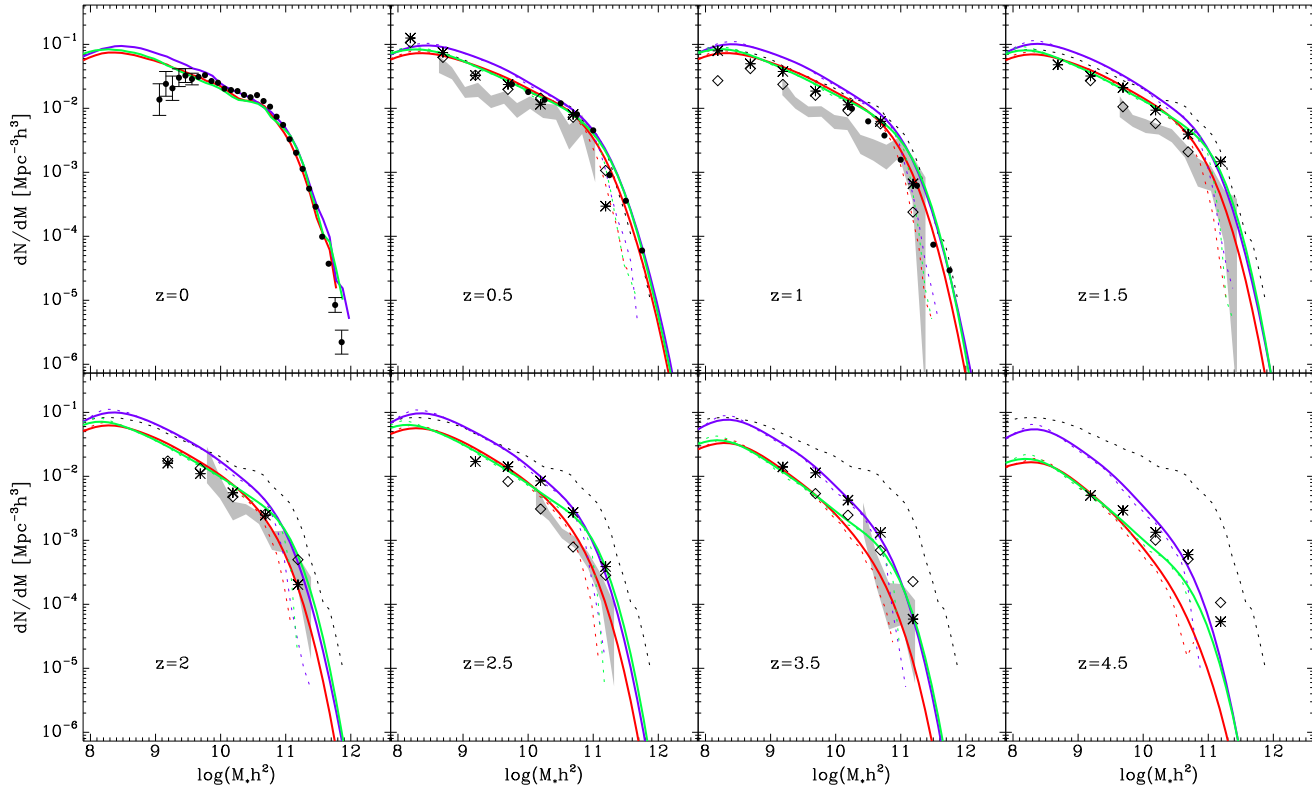


Figure 14. Evolution of the galaxy stellar mass function from $z = 0$ to $z = 4.5$. Model results are shown as solid lines (blue for A1, red for B3, and green for C3). Local data are from Cole et al. (2001) and are repeated as a black dashed curve in the high redshift panels. High redshift data are taken from Drory et al. (2005, symbols) and Fontana et al. (2006, grey shaded areas). Model predictions are shown both with (solid) and without (dotted) convolution with a normal distribution of standard deviation 0.25. At $z = 0$ we consider the mass determinations precise enough to neglect this effect.

be difficult to use galaxy data to distinguish between cosmologies unless the physics of galaxy formation can be independently constrained. Model B3 severely underpredicts the number of massive objects at $z = 4.5$, but even this disagreement may not be significant once cosmic variance and observational uncertainties are taken into account.

Finally, we look at the evolution of clustering to high redshift. Fig. 15 presents spatial 2-point correlation functions at five different redshifts for all resolved subhaloes (for comparison with the lower panel of Fig. 4) and for galaxies in four different stellar mass bins in each of our three “good” galaxy formation models. Perhaps surprisingly, although the result of section 4, that the clustering of resolved subhaloes is very similar in our two cosmologies, is even more accurately true at $z = 1$, it does not hold out to high redshift. For $z > 3$, resolved subhaloes are actually substantially *more* strongly clustered in the WMAP3 cosmology than in WMAP1, despite the fact that the former has a significantly *lower* mass clustering amplitude. This effect is also visible in the galaxy autocorrelations. At the present day our models predict galaxies of all stellar masses to be somewhat more strongly clustered in the WMAP1 cosmology than in the WMAP3 cosmology. Beyond $z = 2$ the opposite is true. By $z = 5$ the effect is quite strong, more than a factor of two in correlation amplitude. These effects may seem surprising, but in fact the corresponding results for dark haloes are easily

obtained if standard analytic models are applied to our two cosmologies. For the convenience of the reader we provide an appendix repeating Mo & White’s (2002) graphical analysis of evolution in the abundance and clustering of halos for these two cases. The large difference in the predicted galaxy clustering properties in the two cosmological model could potentially help to diagnose cosmological parameters. We note, however, that our model is not able to predict reliably high redshift galaxy populations such as Ly- α emitters, ultraluminous infrared galaxies etc. In addition, observational measurements at these redshifts are affected by systematics that are not currently well understood. A rigorous comparison between model predictions and observational measurements at these redshifts is thus still difficult.

6 CONCLUSIONS AND DISCUSSION

We have carried out cosmological structure formation simulations of a Λ CDM Universe for the cosmological parameter sets suggested by the first- and third-year WMAP results. The significant reduction in the best value for the amplitude of matter fluctuations on $8 h^{-1}$ Mpc scale (σ_8) combines with the decrease in the estimate of the scalar spectral index for primordial perturbations (n), and with the lowered matter

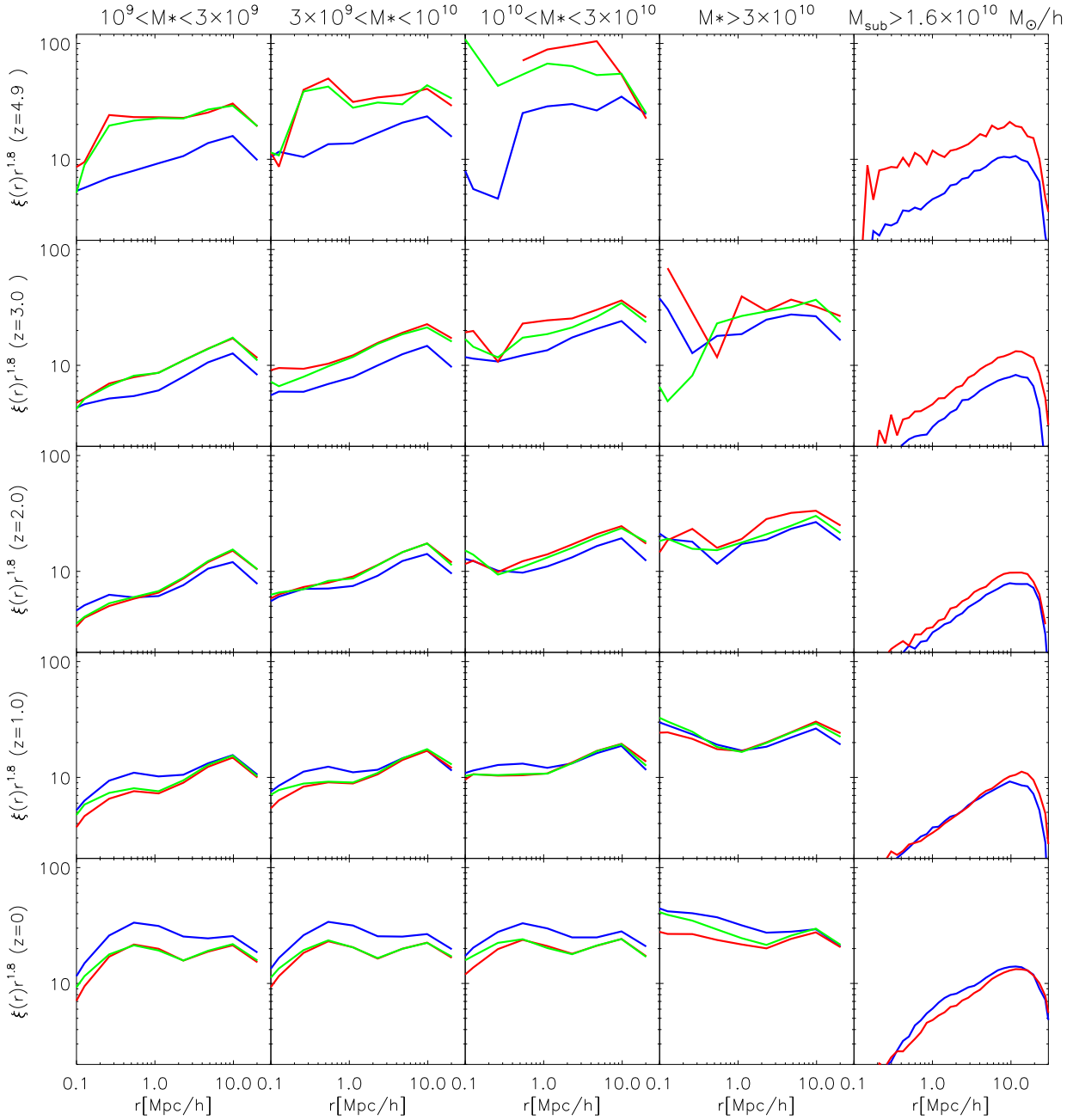


Figure 15. Autocorrelation functions for galaxies and for resolved subhaloes at five different redshifts ($z = 4.9; 3.0; 2.0; 1.0; 0.$). The galaxy results are given for four disjoint ranges in stellar mass, as indicated. (Stellar mass M_* is given in units of M_\odot .) For $M_* > 3 \times 10^{10}$ there are too few galaxies at $z = 4.9$ to get meaningful results, so we leave this panel blank. Different colours in the galaxy panels refer to our different formation models, blue for A1, red for B3, and green for C3. In the subhalo column the colours refer to our two simulations, blue for WMAP1, red for WMAP3. We have multiplied all correlation functions by $r^{1.8}$ to make the differences between the models more visible. Note that r is a comoving coordinate with units of $h^{-1}\text{Mpc}$.

density (Ω_m) to produce a significant delay in structure formation in the WMAP3 case (see Sec. 4).

By coupling our numerical simulations to semi-analytic models for galaxy formation, we have investigated the implications of this delay for the observed properties of galaxies, both at low and at high redshift. Specifically, we have compared the galaxy formation model described in

De Lucia & Blaizot (2007) for the WMAP1 cosmology to two galaxy formation models for the WMAP3 cosmology which use the same physical framework but different efficiency parameters. We find that both new parameter sets can compensate for the delay in structure formation to produce galaxy populations at $z = 0$ which agree with observation just as well as the old model for the WMAP1 cosmology.

The luminosity functions are almost identical, the correlation functions show at most small differences, and offsets in the predicted Tully-Fisher relations are difficult to interpret because disk rotation velocities cannot be predicted reliably to the level of accuracy required.

Pairwise velocity dispersion measurements are sensitive to cluster abundance and therefore differ significantly for the two cosmological models of our study. We have shown that the two WMAP3 models underpredict the measured PVD by more than 100km/s on scales $0.3 < r_p < 2\text{Mpc}/h$, and are lower than the corresponding predictions of the WMAP1 model by 50 ~ 150km/s on all scales.

Substantial differences between the various models appear at high redshift. The delay in the structure formation translates directly into a delay in the global star formation history: at $z \sim 6$ the star formation rates in the models based on WMAP3 are lower than those based on WMAP1 by almost an order of magnitude. As discussed elsewhere, this has important implications for the formation of the first stars, and for reionization. Predictions of our three models for galaxy luminosity and mass functions at high redshift show substantial differences. Unfortunately, the uncertainties in the observed luminosities and masses, combined with large cosmic variance uncertainties, are still too large to place strong constraints on the efficiencies and scalings of the physical processes we model. Somewhat counterintuitively, we find that at high redshift galaxies of given stellar mass are predicted to be substantially more clustered in the WMAP3 cosmology than for WMAP1.

When comparing $z = 0$ correlation functions from our three models to recent observational determinations from the 2dFGRS (Hawkins et al. 2003) and the SDSS (Li et al. 2006), we found interesting and apparently significant differences between the models, particularly for galaxies fainter than ~ -20 in the SDSS r-band. At these magnitudes, our WMAP3 galaxy catalogues provide better agreement with the SDSS data but the opposite is true for galaxies around the knee of the luminosity function. It is important to realise that the reduced mass clustering amplitude implied by the WMAP3 parameters is almost entirely offset by an increase in halo bias, so that predictions for galaxy clustering change very little. At least at separations $r < 20h^{-1}\text{Mpc}$, galaxy clustering is much more sensitive to galaxy formation physics than to cosmological parameters (see also the discussion in van den Bosch et al. 2003). In fact, for almost all of the population properties we have examined, the variations induced by “acceptable” variations in the galaxy formation parameters are at least as large as those produced by the variation in cosmological parameters between WMAP1 and WMAP3. The systematic properties of galaxies and their small-scale clustering should be used to understand how galaxies form, not to constrain cosmology. A similar conclusion was reached by Kauffmann et al. (1999a) who used cruder semianalytic models to show that similar $z = 0$ clustering was predicted in two quite different cosmological models (τCDM and ΛCDM). In this case, however, the predicted evolution to high redshift was different enough to offer a clear way to distinguish the models (Kauffmann et al. 1999b).

In this paper we have shown that varying efficiency parameters within a given framework for modelling galaxy formation can lead to very similar predictions for the evolution

and clustering of galaxies in the WMAP1 and WMAP3 cosmologies. The problem is sufficiently degenerate that a variety of acceptable parameter sets can be found in either cosmology. It may seem unsatisfactory to ‘fine-tune’ model parameters to fit the observational data, but it is interesting that substantially different efficiencies of star formation and feedback are required in the various cases. More detailed observational data on how these processes work in individual systems may therefore shed light on which parameter values are appropriate. In addition, differing efficiencies translate into significantly different predictions at high redshift. More detailed and more statistically precise observations of high-redshift galaxies will be able to distinguish between the models. Once these aspects of the galaxy formation process are better understood, it may indeed be possible to use galaxy surveys to constrain cosmological parameters.

ACKNOWLEDGEMENTS

We thank Volker Springel for providing us with the simulation code GADGET2 and with post-processing software. We thank Cheng Li for help in understanding the SDSS data and for providing the PVD fitting code used in his paper. We thank Lan Wang for providing the HOD galaxy catalogue from her Millennium Simulation model. We also thank J. Blaizot, L. Gao, G. Guzzo and Y. P. Jing for helpful discussions, and an anonymous referee for suggesting the inclusion of the PVD analysis and offering other useful comments. The simulations described in this paper were carried out on the Blade Centre cluster of the Computing Center of the Max-Planck-Society in Garching. The Millennium Simulation data used in this paper are publicly available from <http://www.mpa-garching.mpg.de/millennium>

REFERENCES

- Alvarez M. A., Shapiro P. R., Ahn K., Iliev I. T., 2006, *ApJ*, 644, L101
- Benjamin J., Heymans C., Semboloni E., Van Waerbeke L., et al. 2007, *ArXiv Astrophysics e-prints*
- Binney J., Tremaine S., 1987, *Galactic dynamics*. Princeton, NJ, Princeton University Press, 1987, 747 p.
- Blanton M. R., Brinkmann J., Csabai I., Doi M., Eisenstein D., Fukugita M., Gunn J. E., Hogg D. W., Schlegel D. J., 2003, *AJ*, 125, 2348
- Blanton M. R., Hogg D. W., Bahcall N. A., Brinkmann J., Britton M., Connolly A. J., Csabai I., Fukugita M., et al. 2003, *ApJ*, 592, 819
- Borgani S., Rosati P., Tozzi P., Stanford S. A., Eisenhardt P. R., Lidman C., Holden B., Della Ceca R., Norman C., Squires G., 2001, *ApJ*, 561, 13
- Carlberg R. G., Yee H. K. C., Ellingson E., Abraham R., Gravel P., Morris S., Pritchet C. J., 1996, *ApJ*, 462, 32
- Ciardi B., Ferrara A., White S. D. M., 2003, *MNRAS*, 344, L7
- Cole S., Lacey C. G., Baugh C. M., Frenk C. S., 2000, *MNRAS*, 319, 168
- Cole S., Norberg P., Baugh C. M., Frenk C. S., Bland-Hawthorn J., Bridges T., Cannon R., Colless M., et al. 2001, *MNRAS*, 326, 255

- Colless M., Dalton G., Maddox S., Sutherland W., Norberg P., Cole S., Bland-Hawthorn J., Bridges T., et al 2001, MNRAS, 328, 1039
- Conroy C., Wechsler R. H., Kravtsov A. V., 2007, ArXiv Astrophysics e-prints
- Croton D. J., Springel V., White S. D. M., De Lucia G., Frenk C. S., Gao L., Jenkins A., et. al 2006, MNRAS, 365, 11
- de Bernardis P., Ade P. A. R., Bock J. J., Bond J. R., Borrill J., Boscaleri A., Coble K., Contaldi C. R., et al 2002, ApJ, 564, 559
- de Bernardis P., Ade P. A. R., Bock J. J., Bond J. R., Borrill J., Boscaleri A., Coble K., Crill B. P., et al 2000, Nature, 404, 955
- De Lucia G., Blaizot J., 2007, MNRAS, 375, 2
- De Lucia G., Kauffmann G., Springel V., White S. D. M., Lanzoni B., Stoehr F., Tormen G., Yoshida N., 2004, MNRAS, 348, 333
- De Lucia G., Kauffmann G., White S. D. M., 2004, MNRAS, 349, 1101
- De Lucia G., Springel V., White S. D. M., Croton D., Kauffmann G., 2006, MNRAS, 366, 499
- Drory N., Salvato M., Gabasch A., Bender R., Hopp U., Feulner G., Pannella M., 2005, ApJ, 619, L131
- Feulner G., Bender R., Drory N., Hopp U., Snigula J., Hill G. J., 2003, MNRAS, 342, 605
- Fontana A., Salimbeni S., Grazian A., Giallongo E., Pentericci L., Nonino M., Fontanot F., Menci N., Monaco P., Cristiani S., Vanzella E., de Santis C., Gallozzi S., 2006, A&A, 459, 745
- Gao L., Abel T., Frenk C. S., Jenkins A., Springel V., Yoshida N., 2006, ArXiv Astrophysics e-prints
- Gao L., White S. D. M., Jenkins A., Stoehr F., Springel V., 2004, MNRAS, 355, 819
- Ghigna S., Moore B., Governato F., Lake G., Quinn T., Stadel J., 2000, ApJ, 544, 616
- Giovanelli R., Haynes M. P., da Costa L. N., Freudling W., Salzer J. J., Wegner G., 1997, ApJ, 477, L1+
- Gonzalez A. H., Zabludoff A. I., Zaritsky D., 2005, ApJ, 618, 195
- Hawkins E., Maddox S., Cole S., Lahav O., Madgwick D. S., Norberg P., Peacock J. A., Baldry e., 2003, MNRAS, 346, 78
- Hoekstra H., Mellier Y., van Waerbeke L., Semboloni E., Fu L., Hudson M. J., Parker L. C., Tereno I., Benabed K., 2006, ApJ, 647, 116
- Huang J.-S., Glazebrook K., Cowie L. L., Tinney C., 2003, ApJ, 584, 203
- Iliev I. T., Mellema G., Pen U.-L., Bond J. R., Shapiro P. R., 2007, ArXiv Astrophysics e-prints
- Jing Y. P., Börner G., 2004, ApJ, 617, 782
- Jing Y. P., Mo H. J., Boerner G., 1998, ApJ, 494, 1
- Kauffmann G., 1996, MNRAS, 281, 475
- Kauffmann G., Colberg J. M., Diaferio A., White S. D. M., 1999a, MNRAS, 303, 188
- Kauffmann G., Colberg J. M., Diaferio A., White S. D. M., 1999b, MNRAS, 307, 529
- Kauffmann G., Haehnelt M., 2000, MNRAS, 311, 576
- Kennicutt Jr. R. C., 1998, ApJ, 498, 541
- Kitzbichler M. G., White S. D. M., 2007, MNRAS, pp 75–+
- Lewis A., Weller J., Battye R., 2006, MNRAS, 373, 561
- Li C., Jing Y. P., Kauffmann G., Börner G., Kang X., Wang L., 2007, MNRAS, 376, 984
- Li C., Kauffmann G., Jing Y. P., White S. D. M., Börner G., Cheng F. Z., 2006, MNRAS, 368, 21
- Li G. L., Mao S., Jing Y. P., Mo H. J., Gao L., Lin W. P., 2006, MNRAS, 372, L73
- Martin C. L., 1999, ApJ, 513, 156
- Massey R., Rhodes J., Leauthaud A., Capak P., Ellis R., Koekemoer A., Refregier A., Scoville N., et al 2007, ArXiv Astrophysics e-prints
- Mather J. C., Cheng E. S., Eplee Jr. R. E., Isaacman R. B., Meyer S. S., Shafer R. A., Weiss R., Wright E. L., et al 1990, ApJ, 354, L37
- Mo H. J., Jing Y. P., Börner G., 1993, MNRAS, 264, 825
- Mo H. J., Mao S., White S. D. M., 1998, MNRAS, 295, 319
- Mo H. J., White S. D. M., 2002, MNRAS, 336, 112
- Penzias A. A., Wilson R. W., 1965, ApJ, 142, 419
- Popa L. A., 2006, ArXiv Astrophysics e-prints
- Pozzetti L., Cimatti A., Zamorani G., Daddi E., Menci N., Fontana A., Renzini A., Mignoli M., et. al 2003, A&A, 402, 837
- Reed D. S., Bower R., Frenk C. S., Jenkins A., Theuns T., 2007, MNRAS, 374, 2
- Saracco P., Fiano A., Chincarini G., Vanzella E., Longhetti M., Cristiani S., Fontana A., Giallongo E., Nonino M., 2006, MNRAS, 367, 349
- Schombert J. M., 1988, ApJ, 328, 475
- Schuecker P., Böhringer H., Collins C. A., Guzzo L., 2003, A&A, 398, 867
- Seljak U., Zaldarriaga M., 1996, ApJ, 469, 437
- Smoot G., Bennett C., Weber R., Maruschak J., Ratliff R., Janssen M., Chitwood J., Hilliard L., et al 1990, ApJ, 360, 685
- Somerville R. S., Primack J. R., 1999, MNRAS, 310, 1087
- Spergel D. N., Bean R., Doré O., Nolta M. R., Bennett C. L., Dunkley J., Hinshaw G., Jarosik N., et al 2007, ApJS, 170, 377
- Spergel D. N., Verde L., Peiris H. V., Komatsu E., Nolta M. R., Bennett C. L., Halpern M., Hinshaw G., et. al 2003, ApJS, 148, 175
- Springel V., 2005, MNRAS, 364, 1105
- Springel V., Hernquist L., 2003, MNRAS, 339, 312
- Springel V., White S. D. M., Jenkins A., Frenk C. S., Yoshida N., Gao L., Navarro J., Thacker R., et. al 2005, Nature, 435, 629
- Springel V., White S. D. M., Tormen G., Kauffmann G., 2001, MNRAS, 328, 726
- Tinker J. L., Weinberg D. H., Zheng Z., 2006, MNRAS, 368, 85
- Tinker J. L., Weinberg D. H., Zheng Z., Zehavi I., 2005, ApJ, 631, 41
- van den Bosch F. C., Mo H. J., Yang X., 2003, MNRAS, 345, 923
- van den Bosch F. C., Yang X., Mo H. J., Weinmann S. M., Macciò A. V., More S., Cacciato M., Skibba R., Kang X., 2007, MNRAS, 376, 841
- Wang L., Li C., Kauffmann G., De Lucia G., 2006, MNRAS, 371, 537
- Weinmann S. M., van den Bosch F. C., Yang X., Mo H. J., Croton D. J., Moore B., 2006, MNRAS, 372, 1161
- Yang X., Mo H. J., Jing Y. P., van den Bosch F. C., Chu Y., 2004, MNRAS, 350, 1153

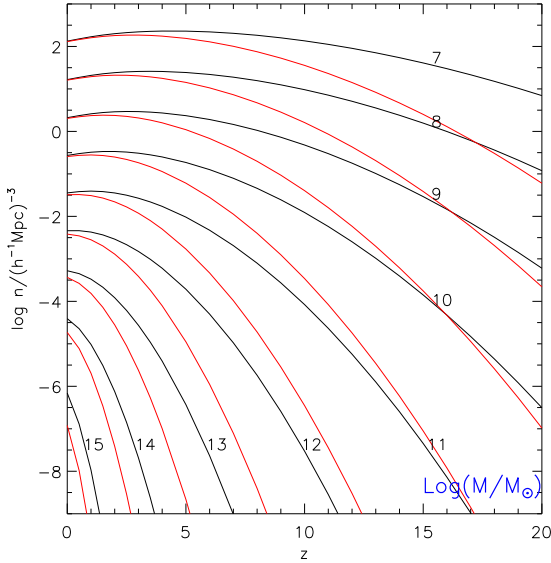


Figure A1. The evolution of the comoving number density of dark matter haloes with mass exceeding a specific value M in our two cosmological models: WMAP1 (black curves) and WMAP3 (red curves). The numbers labelling the black curves indicate the value of $\log(M/M_\odot)$ for the WMAP1 case. See the text for more details.

Zibetti S., White S. D. M., Schneider D. P., Brinkmann J., 2005, MNRAS, 358, 949

APPENDIX A: HALO ABUNDANCE AND CLUSTERING

In this appendix we use the formulae and the graphical presentation scheme of Mo & White (2002) to illustrate how the evolution of halo abundance and clustering differs between our WMAP1 and WMAP3 cosmologies. As in figures 1 and 2 of Mo & White (2002), we present plots of comoving abundance against redshift for halo samples defined by lower mass limits $M_{min}(z)$ corresponding to a variety of halo properties, in particular, for lower limits which correspond at all redshifts to a given halo mass, a given halo virial temperature, a given fraction of the total cosmic mass density, a given clustering strength in comoving units, and a given clustering strength at $z = 0$ for the halo descendents. We refer to Mo & White (2002) for detailed discussion of these quantities and for the relevant formulae.

Figure A1 corresponds to figure 1 of Mo & White (2002). Each curve gives the comoving abundance as a function of redshift of halos more massive than the value indicated by the label. Curves for our WMAP1 parameters are shown in black while curves for our WMAP3 parameters are shown in red. Labels give the decimal logarithm of halo mass in units of solar masses and are placed next to the corresponding WMAP1 curve. Curves are plotted for the same set of mass limits in the two cosmologies, and give almost identical abundances at $z = 0$ for low masses. This can be used to identify the WMAP3 curves at high redshift where they deviate very substantially from the WMAP1 curves.

Springel et al. (2005) showed these theoretical predictions to be in excellent agreement with Millennium Simulation results for $z \leq 10$. At all masses the difference in halo abundance between the two cosmologies increases with the increasing redshift. For $M > 10^{15} M_\odot$ the abundance difference is already almost an order of magnitude at $z = 0$, and the same is true for $M > 10^{12} M_\odot$ at $z = 5$ and $M > 10^8 M_\odot$ at $z = 10$.

In Fig. A2, we give abundance-redshift relations for halo samples defined above lower mass limits $M_{min}(z)$ which correspond to other conditions, as in figure 2 of Mo & White (2002). In each of these plots the two curves of Fig. A1 are repeated as dashed curves. These can be used as a reference to obtain the halo mass corresponding to each point in the abundance-redshift plane.

In the upper left panel of Fig. A2 the solid curves link halo populations containing given fractions F of the total cosmic mass density at each redshift. The labels give F values for the curves they are placed next to. Where no label is given the F value can be inferred from the surrounding curves. Red curves show WMAP3 results for the same F values and lie above the corresponding WMAP1 curves at all redshifts. At $z = 0$ the curves are close enough that it is easy to infer the F value for each red curve by comparing it with the corresponding black curve. For example, for WMAP1 at $z = 0$, one percent of all cosmic mass is in dark halos above a lower mass limit corresponding to abundance $n = 5 \times 10^{-7} h^3 \text{Mpc}^{-3}$, thus $M > 10^{15} M_\odot$ (from Fig. A1). For WMAP3, the $z = 0$ abundance at $F = 0.01$ is about a factor of 2 higher, and the corresponding mass is about 2.5 times smaller. At $z = 5$ the one percent mass point corresponds to $n = 10^{-3} h^3 \text{Mpc}^{-3}$ and $M > 4 \times 10^{11} M_\odot$ for WMAP1, but to $n = 10^{-2} h^3 \text{Mpc}^{-3}$ and $M > 4 \times 10^{10} M_\odot$ for WMAP3.

In the upper right panel of Fig. A2 the solid curves link halo populations at each redshift with virial temperatures T in excess of a given value. Labels give the decimal logarithm of the limiting temperature in Kelvin and are placed next to the curve they refer to. At $z = 0$, there is a close correspondence between WMAP1 and WMAP3 at high abundance. At low abundance (high mass) the WMAP3 curves lie below their WMAP1 counterparts. At $z = 10$, the current best estimate of the reionization redshift, only halos with $M > 8 \times 10^7 M_\odot$ have virial temperatures sufficient to ionize hydrogen ($T > 10^4 \text{K}$) and are thus able to cool their baryonic component effectively. For WMAP1 parameters, the comoving abundance of such halos is $n = 10 h^3 \text{Mpc}^{-3}$ and they contain a fraction $F \sim 0.04$ of all cosmic matter (from the upper left plot of Fig. A2). For WMAP3 parameters, the predicted abundance of such halos drops by about a factor of 6, and the fraction of cosmic matter contained in them drops by about an order of magnitude. This is the reason why reionization is much more difficult to explain (at $z = 10$) for the revised WMAP parameters. Differences of this kind also explain why we get higher global star formation rates at $z \sim 5$ in our model A1 than in our models B3 and C3 (Fig.12) as well as a correspondingly higher stellar mass function in A1 at high redshift (Fig. 14).

In the lower left panel of Fig. A2 the solid curves link halo populations at each redshift which have a given strength of clustering in comoving coordinates as characterized by $\Delta_8(M, z)$, the rms fluctuation in overdensity of haloes more

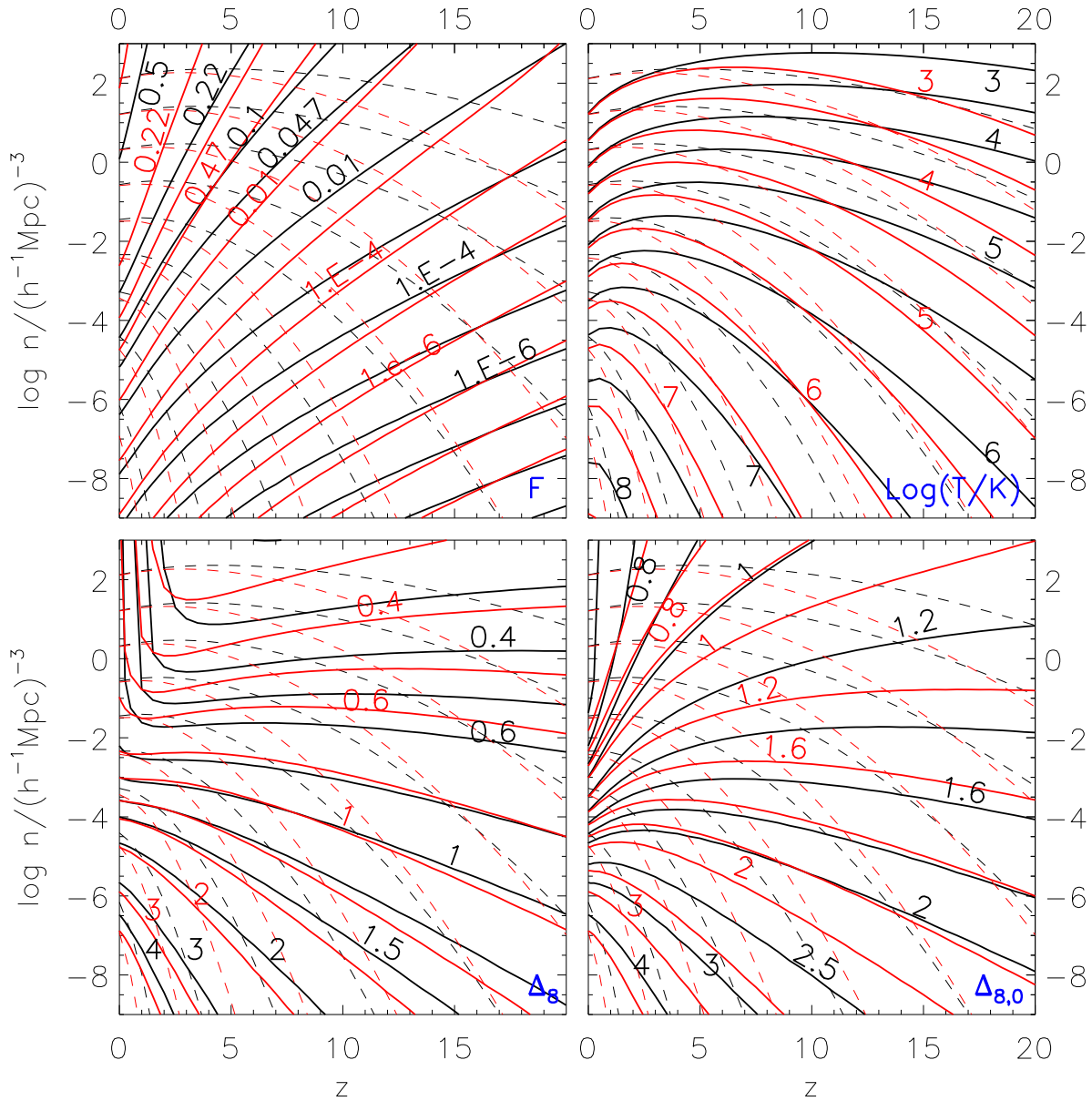


Figure A2. A repeat of figure 2 of Mo & White (2002) but showing results for both WMAP1 (black) and WMAP3 (red) parameters. The limiting mass of the halo population is chosen so as to keep a different quantity constant along a solid curve in each panel: cosmic mass fraction F (top left), minimum virial temperature T (top right), clustering strength Δ_8 (bottom left) and clustering strength of the $z = 0$ descendants $\Delta_{8,0}$ (bottom right). The dashed curves in each panel repeat those of Fig. A1. The black and red numbers label the WMAP1 and WMAP3 curves, respectively. See the text for details.

massive than M at redshift z after smoothing with a spherical top-hat filter of comoving radius $8h^{-1}\text{Mpc}$. As in the other panels, the labels give Δ_8 values for the curves they are placed next to. At redshifts 5 to 10, the WMAP3 curves lie below the corresponding WMAP1 curves at low abundances but above them at high abundances. Comparing the dashed and solid curves in this panel, one sees that at $z = 0$ the clustering strength of halos is very similar in the two cosmologies for all lower limits to halo mass. This is the result visible in the lower panel of Fig. 4. At $z = 5$, however, these same curves show the clustering strength of halos to be substantially stronger in WMAP3 for all limiting halo masses than in WMAP1 (typically by 25 to 40% in Δ_8).

This is the result seen for low-mass (sub)halos in the right column of Fig. 15.

Finally, in the lower right panel of Fig. A2 solid curves link halo populations at each redshift for which the $z = 0$ descendants have a given clustering strength, as indicated by $\Delta_{8,0}$, their present-day value of Δ_8 . As in the other panels, the labels give values of $\Delta_{8,0}$ for the curves they are placed next to. At $z = 0$, the two cosmologies predict nearly identical clustering strengths at intermediate abundances. Mo & White (2002) give a number of examples of how this plot may be used. Here we note that the progenitor population which ends up with a given $z = 0$ clustering strength is

substantially more strongly clustered at high redshift in the WMAP3 cosmology than in the WMAP1 cosmology.

This paper has been typeset from a \TeX / \LaTeX file prepared by the author.